Geomechanics and Engineering, *Vol. 41, No. 5 (2025) 527-542*
https://doi.org/10.12989/gae.2025.41.5.527

Development of similar materials with porous of the coral reef limestone and tunnel deformation failure characteristics analysis in the soft and hard interlayer stratum

Xiangyu Zhang[1a], Lewen Zhang[1b], Fuqiang Li[2c], Jing Wu*[1] and Wenjuan Wu[3d]

[1]*Institute of Marine Science and Technology, Shandong University, Qingdao 266237, Shandong, China*
[2]*The Third Exploration Team of Shandong Coalfield Geologic Bureau, Taian 271000, China*
[3]*Shandong Transportation Institute, Jinan 250102, China*

(*Received February 8, 2025, Revised May 13, 2025, Accepted May 14, 2025*)

Abstract. Coral reef limestone (CRL) exhibits varying sedimentary facies, rock structures, and lithologies at different depths, posing challenges for island engineering construction. This study investigates deformation characteristics of surrounding rock during tunnel excavation in soft-hard interlayered CRL stratum. A novel method for preparing heterogeneous analog materials with prefabricated pores is developed to simulate soft and hard CRL interlayers. Physical model tests under two working conditions examine displacement and stress variations during tunnel excavation. Numerical simulations are subsequently conducted to verify test validity and assess stratum distribution impacts. Key findings include: (1) Prefabricated pore structures effectively replicate CRL's natural heterogeneity. (2) Upper-soft/lower-hard stratum induces significant vault displacement (2.35 mm) and stress concentration (0.82 MPa) due to soft rock compression. (3) Upper-hard/lower-soft configurations cause pronounced arch foot deformation (3.12 mm) from soft rock yielding under overlying hard stratum. (4) Support systems reduce displacements by 14.8% (lining alone) and 33.3% (combined lining-anchor), with enhanced effectiveness in soft CRL. The integrated experimental-numerical approach provides critical insights for tunnel design in heterogeneous CRL formations, demonstrating that support optimization should prioritize lithological interfaces and stress redistribution patterns characteristic of interlayered systems.

Keywords: coral reef limestone; similar material with pores; soft and hard interlayer; surrounding rock stability; tunnel excavation

1. Introduction

In recent years, China's marine construction industry has witnessed vigorous development. With the proposal of the "Belt and Road Initiative" and the "21st Century Maritime Silk Road" initiative, island and reef construction projects have been actively carried out in the country (Tang and Zhu 2025). Coral reef limestone (CRL), as the main component of coral reef rock soil, serves as the foundation and foothold for island and reef construction (Al-Kahtany 2017, Bosellini *et al.* 2021, Ye *et al.* 2021, Zhong *et al.* 2022). Consequently, the development of underground spaces within CRL stratum has become increasingly vital and has become an important support for the development and construction of marine engineering in various countries. (Wild *et al*. 2011, Wang *et al.* 2023a).

The CRL is a composite rock and soil body that forms through the mutual cementation of coral remains, various reef-attached organisms, shellfish, and algae in marine environments following the demise of reef-building coral communities (Huang *et al*. 2024, Xu *et al.* 2024). This formation has undergone the combined effects of geological deposition, biological degradation, and marine dynamics (Jafarian *et al*. 2018, Triantafyllidis and Kimmig 2019). The CRL constitutes the diagenetic portion of the lower coral reef, forming the primary structure of reef islands (Zhang *et al.* 2023a). A large number of reef sediments exist in the marine environment. For example, the South China Sea islands (except Xisha High sharp Rock Island) are all composed of coral reefs. The diagenetic process of CRL preserves the biological characteristics of the internal primary coral skeleton, which is typically characterized by structural heterogeneity and high porosity. These features result in a complex rock structure with significant fragmentation (Wu *et al*. 2023, Zhang *et al*. 2024). In view of the special mechanical characteristics of CRL, fruitful research works on the CRL from the aspects of density, porosity, longitudinal wave velocity, water properties, point load strength index, uniaxial compressive strength, tensile strength, shear strength index, etc., are first analyzed. And then the crack development law and damage evolution

*Corresponding author, Ph.D.
E-mail: jing.wu@sdu.edu.cn
[a]Ph.D. Student
E-mail: zhangxiangyu920@163.com
[b]Professor
E-mail: lewenzhang@sdu.edu.cn
[c]Ph.D.
E-mail: 859918724@qq.com
[d]Ph.D.
E-mail: 2877918380@qq.com

ISSN: 2005-307X (Print), 2092-6219 (Online)

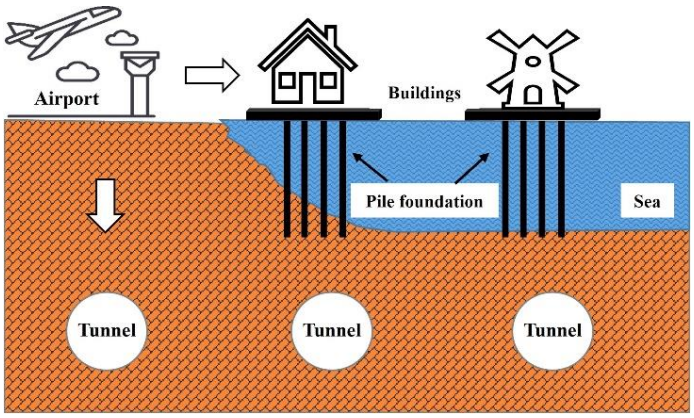

Fig. 1 Present situation and future development trend of the island construction

characteristics of CRL during the failure process are explored combined with the scanning electron microscopy, the acoustic emission, the CT (computerized tomography) scanning and other technical means (Liu *et al*. 2021, Pei *et al.* 2022, Luo *et al*. 2023).

The land reclamation and reef construction on the coral island reefs in the South China Sea is first put into effect out of the national strategy demands of marine development (Wu *et al.* 2020, Wang *et al.* 2022), shown in Fig. 1. The reef constructions mostly adopt the form of shallow foundation in the completed reef projects, which rely on the reinforced blown reef sand as the foundation supporting layer (Zhang and Ye 2021, Zhang *et al.* 2024). The depth of buried construction to be built is getting larger with the development of reef engineering, and the pile foundation relying on the deep limestone stratum as the supporting layer will be the preferred foundation type (Wan *et al.* 2018, Li *et al.* 2022, Zhang *et al.* 2022b). However, the pile foundation design according to the original experience does not conform to its settlement law because of the special mechanical characteristics of CRL, which will cause some engineering accidents. In that case, a series of studies on the pile foundations of coral reefs began to be conducted (Wang *et al.* 2023a).

The development of underground space in CRL stratum is becoming a key trend in reef engineering. As reef engineering advances, the stability of surrounding rock is essential for safe tunnel excavation (Zhu *et al.* 2003, Zhang *et al.* 2017, He *et al.* 2022, Chang *et al.* 2025, Hu *et al.* 2025, Yin *et al.* 2025). In the author's prior research, physical model tests and numerical simulations were conducted. These studies focused on the stability of surrounding rock during tunnel excavation in CRL. The results revealed displacement and stress patterns during the excavation process (Zhang *et al.* 2022a). Nevertheless, the CRL during the growth has undergone several sedimentary cycles because of the influence of the geological environment and tropical marine environment (Bosellini 1998, Raczynski *et al.* 2017). The CRL in different depths is formed in different dynamic environments, so it has various sedimentary facies, rock structures and types (Nakamori *et al.* 1995, Burton *et al.* 2001, Al-Kahtany 2017). It is inevitable to cross the alternating occurrence of the soft and hard CRL in the process of tunnel excavation.

The model test under the condition of satisfying the similarity law can accurately simulate the construction process and reveal the damage and failure characteristics of surrounding rock (Xu *et al.* 2017, Zhao *et al.* 2021, Sun *et al.* 2023, Wang *et al.* 2023b, Zhang *et al.* 2023b, Li *et al.* 2025). However, researches on rock similar materials in physical model tests mainly focuses on terrigenous rocks (Seo and Chung 2023, Zhou *et al.* 2024), and the development of similar materials for CRL is limited.

Given the complexity and variability of CRL, conducting both physical model tests and numerical simulations of tunnel excavation within CRL stratum comprising soft and hard interlayers is essential. These approaches enable the simulation of real-world tunnel excavation processes, providing more accurate and reliable data for engineering design. This, in turn, facilitates the precise prediction and assessment of potential challenges and issues that may arise during tunnel construction in CRL stratum.

2. Characteristics and stratum distribution of the CRL

The CRL is a complex rock body formed after long sedimentary evolution and geological processes by cementing the calcareous coral skeletons with other calcareous organisms such as algae and shellfish. Based on the structural characteristics and components of CRL, the South China Sea Institute of Oceanology of the Chinese Academy of Sciences divided it into four types, coral skeleton limestone (CSL), coral boulder limestone (CBL), coral gravel limestone (CGL) and coral calcarenite limestone (CCL), shown in Fig. 2(a). The CRL not only inherits the calcareous skeleton, growth line, biological pore and other structural characteristics of protists, but also is full of pores dissolved by the seawater (Fig. 2(b)), so the CRL has the characteristics of complex structure and heterogeneity.

Taking the island reefs of the South China Sea as a case study, the region lies at the convergence of three major tectonic plates: the Pacific, Eurasian, and Indian plates. The geological setting is highly complex, shaped by the relative movement and interaction of these plates. This dynamic

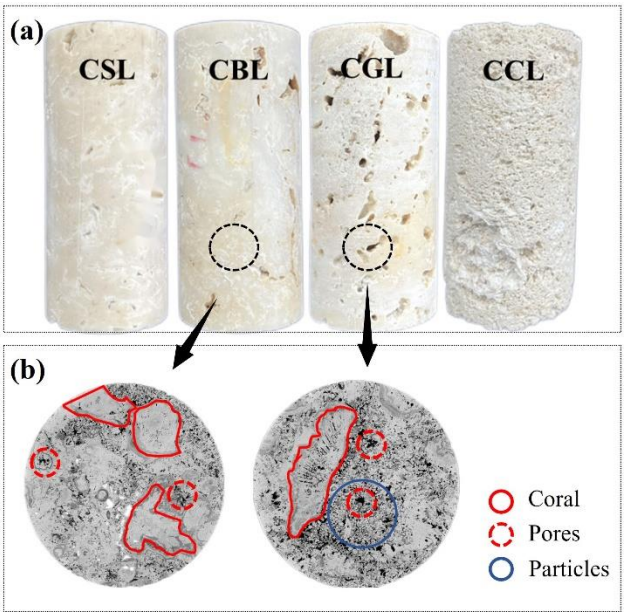

Fig. 2 Characteristics and classification of coral reef limestone: (a) Four types of CRL and (b) Internal structural characteristics of CRL

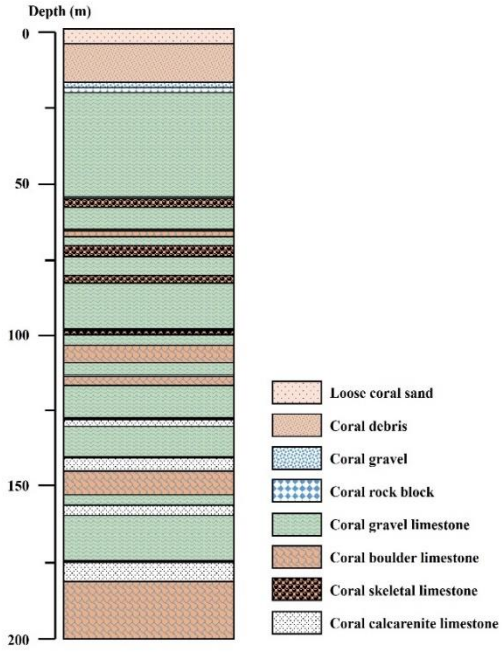

Fig. 3 Stratigraphic distribution of an island reef in the South China Sea (Meng *et al*. 2022)

tectonic environment, combined with the region's distinct diagenetic history, results in significant variation in the physical and mechanical properties of the CRL. The strength of CRL varies markedly; some types are several times stronger than others, with certain varieties being up to dozens of times more robust. Specifically, the uniaxial compressive strength of dry CRL ranges from 1.10 to 38.56 MPa, while that of saturated CRL varies between 0.86 and 49.24 MPa.

Taking the island reefs of the South China Sea as a case study, the region lies at the convergence of three major tectonic plates: the Pacific, Eurasian, and Indian plates. The geological setting is highly complex, shaped by the relative movement and interaction of these plates. This dynamic tectonic environment, combined with the region's distinct diagenetic history, results in significant variation in the physical and mechanical properties of the CRL. The strength of CRL varies markedly; some types are several times stronger than others, with certain varieties being up to dozens of times more robust. Specifically, the uniaxial compressive strength of dry CRL ranges from 1.10 to 38.56 MPa, while that of saturated CRL varies between 0.86 and 49.24 MPa.

Table 1 Values of basic physical and mechanical parameters of soft and hard CRL

Material type	Density (g/cm^3)	Young modulus (GPa)	Poisson ratio	Frictional angle (°)	Cohesion (MPa)	Tensile strength (MPa)
Hard CRL	2.5	12.9	0.27	40	1.67	1.56
Soft CRL	1.09	7.9	0.23	44	1.05	0.88

The influence of the geological environment and tropical marine environment caused coral reefs to undergo several sedimentary cycles during their development process. The CRL at different depths is formed in different dynamic environments, resulting in different sedimentary facies, rock structures, and rock types. Fig. 3 shows the stratigraphic distribution of an island reef. The depth of 0~21.38 m is respectively loose coral sand layer, coral gravel layer, coral debris layer and coral rock block layer. The depth of 21.38 m ~110.88 m is respectively skeleton limestone, boulder limestone, and gravel limestone. The depth of 110.88 m to 200.88 m is respectively boulder limestone, gravel limestone, and calcarenite limestone.

In this paper, the CRL is simplified into two types of soft and hard in the physical model test and numerical simulation. It is based on the vertical zonation phenomenon of alternating soft and hard interlayers in the CRL body, which is the overall macroscopic reflection of the uneven development degree of pores, varying strength, and structural disorder. The mechanical behavior of the tunnel excavation in the CRL stratum of soft and hard interlayer can be more concentrated through simplification, so as to provide theoretical support and engineering guidance for a wider range of reef underground engineering. The values of basic physical and mechanical parameters of soft and hard CRL selected in the paper are summarized in Table 1.

3. Development of similar materials with pores

The development of similar materials that meet the required similarity scale is essential for the success of physical model tests. In this study, the similarity relationships considered in the model tests include density, uniaxial compressive strength, tensile strength, elastic modulus, Poisson's ratio, and the size of the physical model. Based on the testing apparatus and the selection of raw materials, the geometric similarity ratio between the prototype and the model is set at 50. Additionally, the density similarity ratio is maintained at 1, while the similarity ratios for stress, displacement, compressive strength, and elastic modulus are all set at 50. The derivation process of the similarity ratio is shown as Eqs. (1)-(4).

(1) The similarity relation of stress similarity scale C_σ, bulk density similarity scale C_γ and geometric similarity scale C_L is as follows

$$C_\sigma = C_\gamma C_L \tag{1}$$

(2) The similarity relation of displacement similarity scale C_δ, geometric similarity scale C_L and strain similarity scale C_ε is as follows

$$C_\delta = C_\varepsilon C_L \tag{2}$$

(3) The similarity relation of stress similarity scale C_σ, elasticity modulus similarity scale C_E and strain similarity scale C_ε is as follows

$$C_\sigma = C_\varepsilon C_E \tag{3}$$

(4) The model test also requires that the similarity scales of all dimensionless physical quantities (such as strain, internal friction angle, internal friction coefficient, Poisson's ratio, etc.) should be equal to 1.

$$C_\varepsilon = C_\phi = C_\mu = 1 \tag{4}$$

Table 2 Final determined ratio of similar materials for the hard CRL

Material	Quartz sand	Barite powder	Cement	Gypsum powder	Water
Ratio	35%	35%	16%	4%	28%

Table 3 Physical and mechanical parameter values of hard CRL and its similar material

Material type	Density (g/cm^3)	Compressive strength (MPa)	Tensile strength (MPa)	Elastic modulus (GPa)	Poisson ratio
Hard CRL	2.5	40	1.56	12.9	0.27
Similar material	2.5	0.8	0.032	0.26	0.26

3.1 Similar material of hard CRL

Through a literature review and analysis of the physical and mechanical properties of CRL, quartz sand, barite powder, high-strength gypsum, and cement are selected as raw materials (Fig. 4(a)). These materials are mixed with water to prepare a similar material that matches the characteristics of hard CRL. The final mix ratio of the similar material for hard CRL is determined through numerous proportioning and mechanical tests. The results are shown in Table 2. The physical and mechanical parameter values of both hard CRL and its similar material are presented in Table 3.

3.2 Similar material of soft CRL

To simulate the pore structure of CRL, an innovative method was used. Prefabricated ice models of different sizes are added during the preparation of the similar

(a) Raw materials

(b) Prefabricated ice moulds and standard test block moulds

Fig. 4 Configuration processes of similar material

Fig. 5 Similar materials of CRL with prefabricated pores

material. The key idea behind this method is to use the gaps formed by the melting ice to represent the pore structure of CRL. This approach helps improve the geological similarity of the material. The specific steps in the process are as follows.

Firstly, ice moulds (Fig. 4(b)) of different sizes are designed according to the pore structure characteristics of CRL. These prefabricated ices are then added to the raw material in a certain proportion during mixing. The ice has not melted before the material solidifies because of its fast solidification rate, thus forming pores. Pores of different sizes will be formed after ice melted, which can simulate the distribution of pores in the CRL.

To ensure uniformity and consistency in the pore structure, the mixture of ice and raw materials must be homogenous, thereby achieving an even distribution of pores throughout the material. Fig. 5 shows similar materials of CRL with prefabricated pores. It can be found that the pore structure of similar materials has strong non-uniformity, which is consistent with the pore structure characteristics of CRL.

The porosity of similar materials can be calculated by the volume method. Since the density of similar materials of hard CRL without prefabricated pores is determined, the

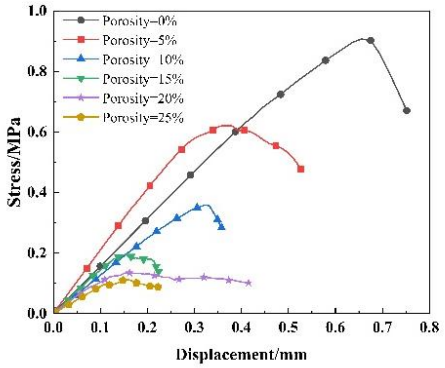

Fig. 6 Stress-strain curves of the similar materials of CRL with different porosity

difference between similar materials of soft CRL with prefabricated pores and similar materials of hard CRL is the final porosity ratio after solidification and curing. The stress-strain curves of the similar materials of CRL with different porosity are shown in Fig. 6 and the similar material of soft CRL is prepared by selecting the material ratio with 15% porosity in this paper.

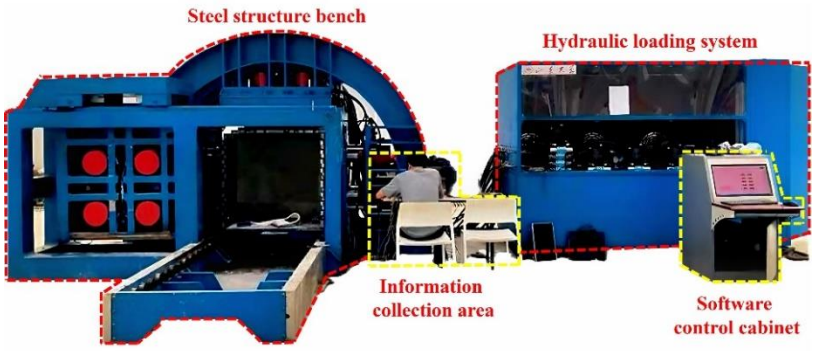

Fig. 7 Fully automated true-triaxial geomechanical test system

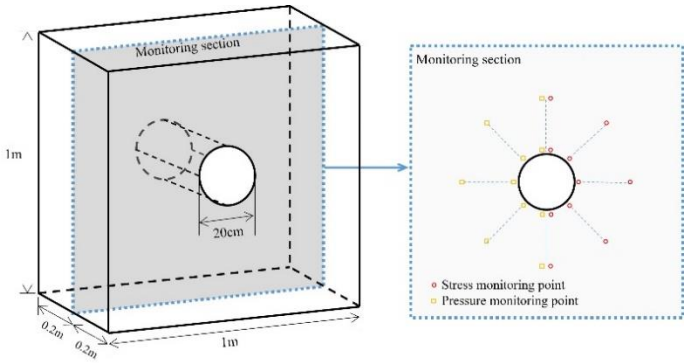

Fig. 8 Model schematic diagram and arrangement of monitoring points

4. Physical model test of tunnel excavation in the CRL stratum of soft and hard interlayer

4.1 Physical model test scheme of tunnel excavation

The study utilized the fully automated true-triaxial geomechanical test system developed by Shandong University. This system comprises a steel structure bench, a software control cabinet, and a hydraulic loading system, as illustrated in Fig. 7. A circular tunnel with a diameter of 10 meters was excavated at a depth of 200 meters for the model test. The geometric similarity ratio for the test was set at 1:50. The model dimensions are designed as 1 m × 1 m × 0.4 m, with pressure applied uniformly to the top and around the entire model. All surfaces are fixed boundaries.

To investigate the effect of soft and hard interlayers on the displacement and stress changes in the surrounding rock during tunnel excavation, two distinct model test conditions are designed. In these conditions, layers of soft CRL (0.5 m thick) and hard CRL (0.5 m thick) are alternately arranged, one above the other. The model schematic and the configuration of monitoring points are presented in Fig. 8.

A monitoring section with eight measuring lines was arranged 20 cm along the excavation direction of the tunnel. The test used high-precision displacement meters and micro soil pressure boxes for monitoring. Monitoring points are strategically placed at critical locations along the tunnel's surrounding rock, including the arch vault, spandrel, haunch, foot, and bottom. An additional monitoring point was positioned one tunnel diameter away from the excavation.

4.2 Making and excavation of the physical model

The physical model is created using layering compaction and air-dry curing. The specific steps are as follows:

1) The similar materials are weighed and mixed according to the designed ratio. They are then filled into the mold to the required height.

2) Slots are cut at the calibrated positions in the model to accommodate the monitoring components and wires. After this, more material is added to complete the model body.

3) After 28 days of curing, the templates are removed. The model is then placed in the test system, and the monitoring components are connected to the computer, preparing for the subsequent loading.

The model fabrication process is illustrated in Fig. 9. The designed load is applied to the model using a hydraulic loading system and is sustained for 24 hours before tunnel excavation begins. To more accurately replicate the actual tunnel excavation process and analyze stress and displacement changes, the bench method is employed. Excavation is carried out in 20 stages, with each stage involving a 2 cm cyclic excavation. During each step, the upper section is excavated first, followed by the lower section, until the tunnel is fully excavated.

4.3 Displacement and stress change laws of the model test condition 1

The model test condition 1 is the tunnel excavation in

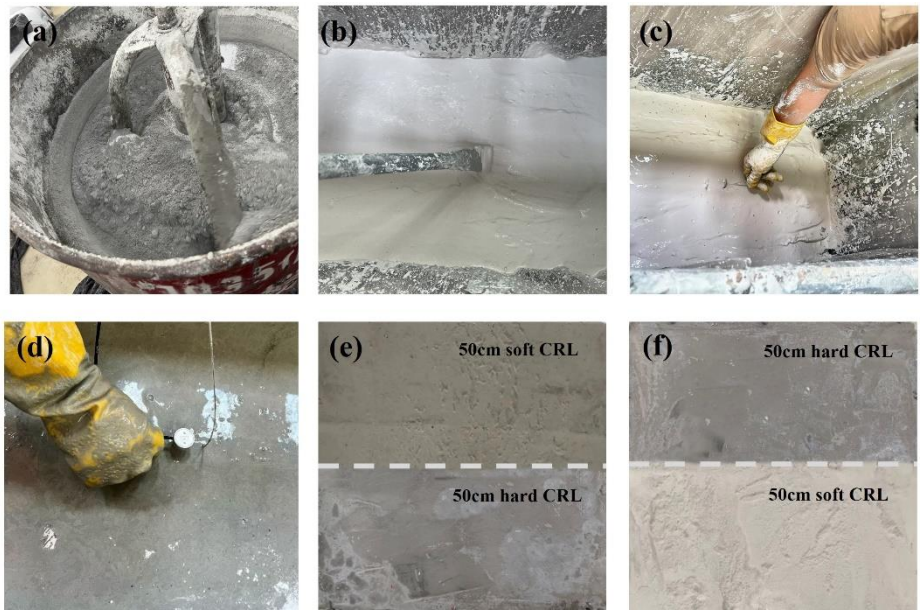

Fig. 9 Model fabrication process: (a) Mixing material, (b) Layered pouring, (c) Burying displacement meter, (d) Burying pressure box, (e) Model 1 and (f) Model 2

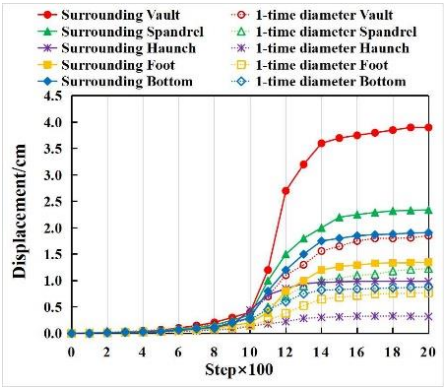

Fig. 10 Displacement change curves of model test condition 1

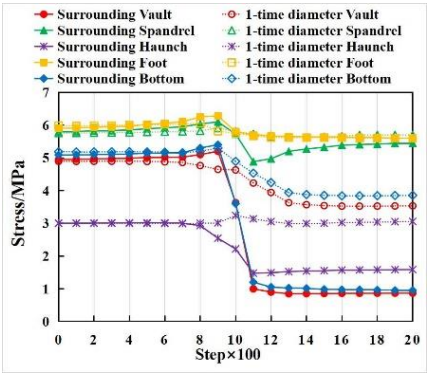

Fig. 11 Stress change curves of model test condition 1

the CRL stratum of soft and hard interlayer. The stratum distribution is 25m soft limestone and 25m hard limestone from top to bottom.

4.3.1 Displacement change laws of the surrounding rock

In model test condition 1, the displacement direction for all monitoring points is defined as the positive direction towards the tunnel's center. The displacement change curves for the surrounding rock in the actual project are presented in Fig. 10(a), derived by applying the similarity ratio conversion.

The displacement curves in Fig. 10 indicate that, before the excavation of the monitoring section, the displacement meters already register deformation in the surrounding rock. This is due to the disturbance of the original equilibrium by the excavation, which triggers a redistribution of internal stress within the rock mass. This stress redistribution impacts both the excavated and unexcavated portions of the surrounding rock. Consequently, the displacement and deformation of the rock mass unfold in three distinct stages:

1) Initial displacement and deformation of the front rock mass.

2) A sharp increase in displacement and deformation in the exposed surrounding rock.

3) Stabilization of displacement and deformation in the surrounding rock.

From model test condition 1, the average displacements of the tunnel surrounding rock are as follows: 3.9 cm at the vault, 2.34 cm at the spandrel, 0.98 cm at the haunch, 1.35 cm at the foot, and 1.91 cm at the bottom. The average displacements at a distance of one tunnel diameter away are: 1.85 cm at the vault, 1.23 cm at the spandrel, 0.32 cm at the haunch, 0.77 cm at the foot, and 0.88 cm at the bottom.

The greatest displacement occurs at the vault, followed by the bottom, while the haunch experiences the smallest displacement during tunnel excavation. On average, the displacement at one tunnel diameter away is 51.8% smaller than that observed in the surrounding rock at the tunnel.

4.3.2 Stress change law of the surrounding rock

The stress directions at all monitored points are oriented towards the center of the tunnel, and the compressive

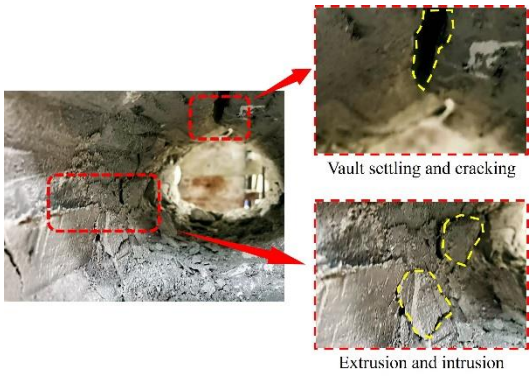

Fig. 12 Test phenomenon of model test condition 1

stresses are recorded as negative values. The stress change curves for the surrounding rock in the actual project are presented in Fig. 11, derived through the similarity ratio conversion.

The stress change curves in Fig. 11 illustrate that, during tunnel excavation, the stress at the arch vault, haunch, and bottom follows a zigzag pattern. Initially, the stress remains stable. As the excavation approaches the monitoring section, stress at each point begins to decrease, and the rate of stress release increases. Once the excavation reaches the monitored section, the stress drops sharply, the release rate escalates, and then stabilizes. In contrast, stress at the arch spandrel and foot increases, with the stress curves showing a gradual rise.

From model test condition 1, the average stress release rates of the surrounding rock are as follows: 80.79% at the vault, 41.89% at the haunch, and 79.47% at the bottom. At the arch spandrel and foot, the stress increases by 3.44% and 4.27%, respectively. The stress release rates at a distance of one tunnel diameter from the excavation are: 20.59% at the vault, 12.05% at the spandrel, 18.26% at the haunch, 8.91% at the foot, and 2.98% at the bottom.

The stress change patterns at each monitoring point exhibit a trend similar to that of displacement changes, as shown in Figs. 10 and 11. As displacement increases, stress decreases, and the rate of stress release rises. This redistribution of stress drives displacement changes, and in turn, the changes in displacement further influence stress redistribution. This cyclical process continues until the surrounding rock reaches a new stable state.

The highest stress release rates are observed at the vault, haunch, and bottom. At the arch spandrel and foot, stress initially decreases and then increases. This behavior occurs because the tunnel excavation disrupts the original stress equilibrium, causing a redistribution of stress in the surrounding rock. The softer upper rock releases stress first, leading to greater displacement at the vault and spandrel. As deformation progresses, the softer upper rock is compressed by the harder lower rock, resulting in an increase in stress. This could potentially lead to further failure of the surrounding rock, as illustrated in Fig. 12.

4.4 Displacement and stress change laws of the model test condition 2

Model test condition 2 involves tunnel excavation through the CRL stratum consisting of alternating soft and hard limestone layers. The stratigraphic sequence includes 25 meters of hard limestone followed by 25 meters of soft limestone, from top to bottom.

The average displacement of the tunnel surrounding rock, derived from the displacement change curves in Fig. 13(a), is as follows: 3.26 cm at the vault, 1.93 cm at the spandrel, 1.3 cm at the haunch, 2.14 cm at the foot, and 3.44 cm at the bottom. At a distance of two tunnel diameters from the excavation, the average displacement values are: 1.33 cm at the vault, 1.02 cm at the spandrel, 0.5 cm at the haunch, 1.06 cm at the foot, and 1.46 cm at the bottom. This indicates that the displacement at two tunnel diameters is, on average, 58% lower than the displacement at the surrounding rock of the tunnel.

The average stress release rates of the surrounding rock, also extracted from Fig. 13(b), are as follows: 84.42% at the vault, 17.22% at the spandrel, 63.06% at the haunch, and 85.07% at the bottom. In contrast, the stress at the arch foot increases by 2.10%. At one tunnel diameter away from the excavation, the stress release rates are: 38.26% at the vault, 5.22% at the spandrel, 14.7% at the haunch, 0.77% at the foot, and 37.54% at the bottom.

It can be seen combined with the test phenomenon shown in Fig. 14 that the arch spandrel is subjected to greater lateral pressure due to the weight and displacement of the upper hard rock, which may cause the hard rock at the arch spandrel to fracture or spread cracks. The soft

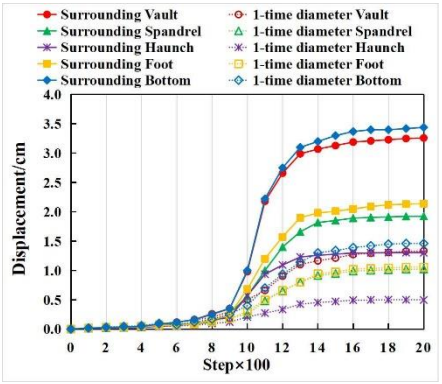

(a) Stress change curves

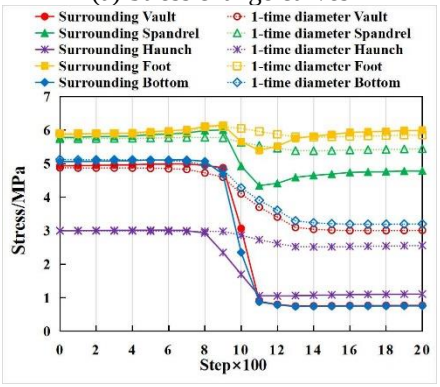

(b) Stress change curves

Fig. 13 Displacement and stress change curves of model test condition 1

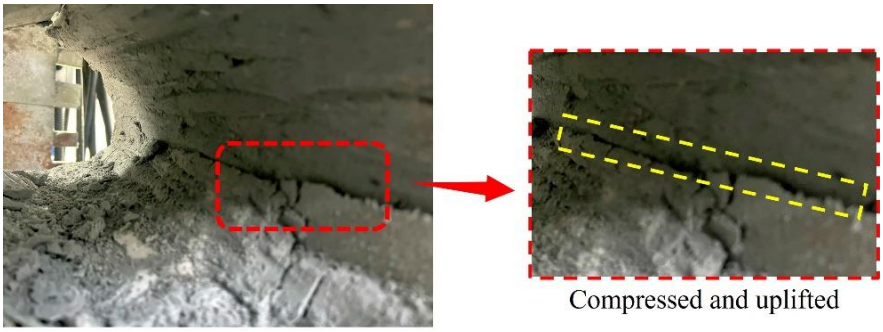

Fig. 14 Test phenomenon of model test condition 2

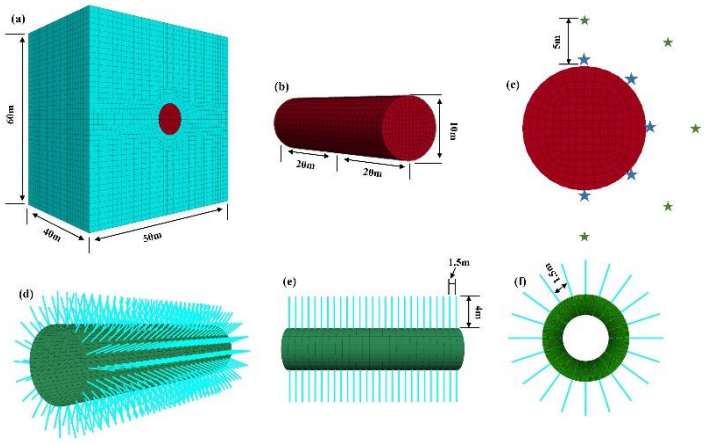

Fig. 15 Numerical model of tunnel excavation: (a) Model size, (b) Tunnel shape and size, (c) Arrangement of monitoring points, (d) Lining and anchor bolt support, (e) Bolt length and longitudinal distribution spacing and (f) Bolt distribution spacing on one section

rock of the arch foot will uplift and occur lateral displacement because of the loss of support after excavation. The deformation at the arch foot may be more significant due to the poor strength and stability of the soft rock, especially under the weight of the upper hard rock.

5. Numerical simulation of tunnel excavation in the CRL stratum of soft and hard interlayer

5.1 Model establishment

The following assumptions are applied in the numerical calculation of the model (Liu *et al.* 2022, Chen *et al.* 2024):

1) The rock mass is treated as a homogeneous and isotropic equivalent continuous medium.

2) An elastic-plastic mechanical model is employed to characterize the deformation of the rock mass.

3) The deformation behavior of the rock mass adheres to the Mohr-Coulomb failure criterion.

The numerical model represents a circular tunnel with a 10-meter diameter, excavated at a depth of 200 meters, as illustrated in Fig. 15. To accurately simulate the effects of tunnel excavation on the surrounding rock mass, the model dimensions are set to 60 m × 60 m × 40 m. The tunnel length is 40 meters, and the excavation process is divided into 20 incremental steps.

Table 4 Working conditions

Conditions	Geological condition	Support methods
1	Soft-Hard	No support Lining Lining and Cable
2	Hard-Soft	No support Lining Lining and Cable

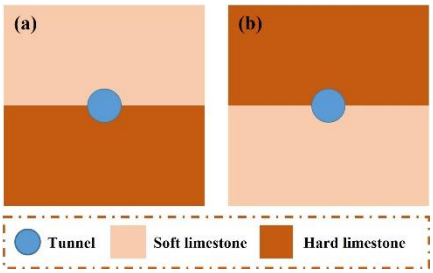

Fig. 16 Two working conditions of numerical simulation

Two different stratigraphic configurations of CRL are designed similar to the model test, as shown in Fig. 16. The tunnel excavation is analyzed under three distinct support scenarios: no support, lining support, and both lining and anchor bolt support. For each stratigraphic condition, the

Table 6 Parameter values of lining

Parameter	Density (g/cm^3)	Thickness (m)	Young modulus (GPa)	Poisson ratio	coupling-stiffness -normal	coupling-stiffness -shear
Value	2.4	0.6	30e9	0.2	8e8	8e8

Table 7 Parameter values of anchor bolt

Parameter	Young modulus (GPa)	Cross-sectional-area (m^2)	Yield-tension (N)	Yield-compression (N)
Value	200e9	3e-4	510e9	345e9

monitoring section is positioned at a depth of 20 meters. Displacement and stress are monitored at critical points along the tunnel's surrounding rock, including the arch vault, spandrel, haunch, foot, and bottom, as well as at a distance of one tunnel diameter away. A summary of the calculation scenarios is provided in Table 4.

5.2 Calculation parameter

5.2.1 Basic parameters of the surrounding rock

Different types of CRL differ greatly in density and strength because of the special characteristics of marine diagenesis. The basic physical and mechanical indexes of CRL are summarized. Taking an island reef as an example, the natural density of CRL is 1.09-2.60 g/cm^3. The uniaxial compressive strength of dry CRL is 1.10 ~ 38.56 MPa, and that of saturated CRL is 0.86 ~ 49.24 MPa. The tensile strength of dry CRL is 0.94 ~ 2.65 MPa, and that of saturated CRL is 0.88 ~ 7.75 MPa. The cohesion is 0.50 ~ 7.34MPa, and the internal friction Angle is 26.5° ~ 71.0°.

The values of basic physical and mechanical parameters of soft and hard CRL in the numerical calculation are summarized in Table 5.

5.2.2 Parameters of lining and anchor bolt

In accordance with the "Technical Code for Engineering of Ground Anchorages and Shotcrete Support," the tunnel lining is designed with a thickness of 60 cm, using C30 reinforced concrete. For the numerical simulations, the Liner structural unit in FLAC 3D is employed, as depicted in Fig. 14(d). In the case of tunnel excavation with a span of approximately 10 meters within this stratum, the anchor bolts are made from high-strength rebar, measuring 25 cm × 4500 cm, with a spacing of 1.5 m × 1.5 m. The elastic modulus of the bolts is 200 GPa, while the tensile strength and yield strength are 510 MPa and 345 MPa, respectively. A total of 27 rows of bolts are used, with each row containing 20 bolts, arranged according to the specified spacing.

The parameter values for the lining and anchor bolts used in the numerical model are provided in Table 6 and Table 7.

5.2.3 Settings of load and boundary condition

This study investigates a tunnel located at a burial depth of 200 meters, with an overlying seawater depth of 100 meters. The vertical pressure in the area results from the combined effects of seawater pressure and the gravitational force of the surrounding rock mass. The lateral pressure coefficient is assumed to be 0.6. Because the depth of this stratum is relatively shallow, the rock mass is in a normal consolidation state and there is no significant tectonic stress. According to the calculation of the theoretical formula of the internal friction Angle, the lateral pressure coefficient is close to 0.6, which is in line with the empirical range of weakly cemented stratum. Consequently, the vertical pressure at the tunnel's crown is 5 MPa, while the horizontal pressure is 3 MPa.

The entire model is subjected to a vertical gravity field of 10 N/kg. The six faces of the numerical model, namely the top, bottom, left, right, front and back, are all set as fixed boundaries. Initially, the in-situ stress is applied to the model. Once the equilibrium of the initial in-situ stress is achieved, the tunnel excavation simulation is then initiated.

6. Numerical calculation results of tunnel excavation

6.1 Numerical calculation results analysis of the working condition 1

The working condition 1 is the tunnel excavation in the CRL stratum of soft and hard interlayer and the stratum distribution is 30 m soft CRL and 30 m hard CRL in the z direction, which is consistent with the model test condition 1. The tunnel excavation is also carried out under the three conditions: no support, lining support, lining and anchor bolt support.

6.1.1 Displacement results analysis of the tunnel surrounding rock

As an example, the numerical simulation of tunnel excavation without support is presented. The displacement cloud maps for both the excavation process and the completed tunnel are shown in Fig. 17.

As shown in Fig. 17, the displacement of the surrounding rock during tunnel excavation is primarily concentrated at the arch vault, where the soft rock is located. The surrounding rock from the arch vault to the arch haunch moves downward in the vertical direction, with displacement gradually decreasing. From the arch haunch to the arch bottom, the surrounding rock moves upward in the vertical direction, showing a gradual increase. This results in the settlement of the arch vault and the uplift of the arch bottom, a phenomenon commonly observed

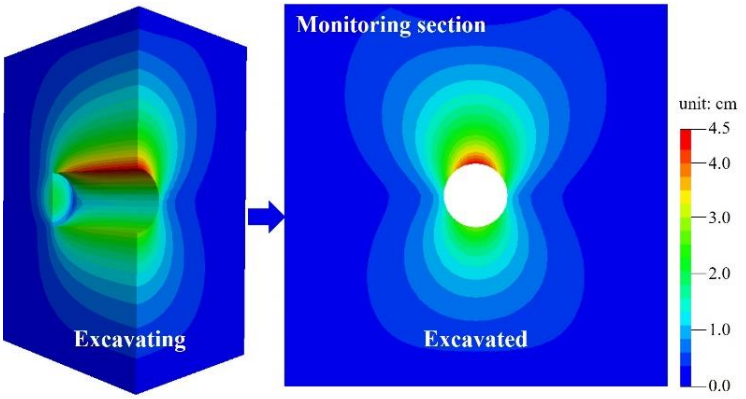

Fig. 17 Displacement cloud maps of tunnel excavating and tunnel excavated

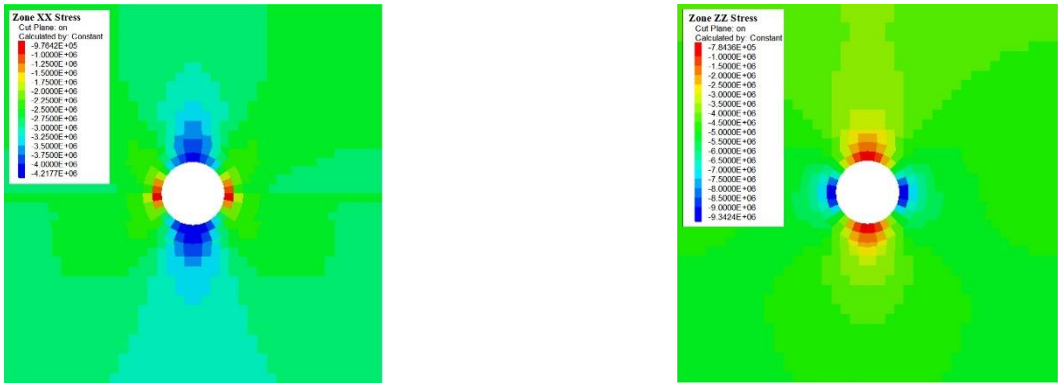

(a) Vertical (b) Horizontal

Fig. 18 Vertical and horizontal stress cloud images of the model monitoring section

Table 8 Final displacements of the surrounding rock in working condition 1

Support method	Location	Vault (cm)	Spandrel (cm)	Haunch (cm)	Foot (cm)	Bottom (cm)
No support	Around tunnel	4.02	2.44	1.09	1.50	2.46
	1-time tunnel diameter	2.14	1.37	0.35	0.85	1.29
Liner	Around tunnel	3.52	2.05	0.69	1.25	2.15
	1-time tunnel diameter	1.88	1.14	0.18	0.70	1.14
Liner and cable	Around tunnel	2.39	1.43	0.42	0.96	1.76
	1-time tunnel diameter	1.45	0.88	0.10	0.54	0.98

in actual engineering projects.

The final displacement values at the monitoring points during tunnel excavation are presented in Table 8.

Table 8 lists the displacement results of the numerical simulation under working condition 1. When no support measures are taken for the tunnel excavation, the displacements around the tunnel are as follows: the vault is 4.02 cm, the spandrel is 2.44cm, the haunch is 1.09 cm, the foot is 1.50 cm and the bottom is 2.46 cm. The average displacements of 1-time tunnel diameter are as follows: the vault is 2.14 cm, the spandrel is 1.37 cm, the haunch is 0.35 cm, the foot is 0.85 cm, and the bottom is 1.29 cm. Compared with no support measures, the average displacement around the tunnel is reduced by 19% when only lining support is adopted, and 41.4% when the lining and bolt support is adopted.

6.1.2 Stress results analysis of the tunnel surrounding rock

As an example, the numerical simulation of tunnel excavation without support is used to generate stress distribution cloud images, which depict the stress in both vertical and horizontal directions at the model's monitoring section after excavation, presented in Fig. 18.

As shown in Fig. 18, during tunnel excavation in working condition 1, the vertical stress significantly decreases at the arch vault and arch bottom. At the arch haunch, the horizontal stress also significantly decreases. This indicates a stress release phenomenon in the surrounding rock.

The stress release rates at the monitoring points after tunnel excavation are presented in Table 9.

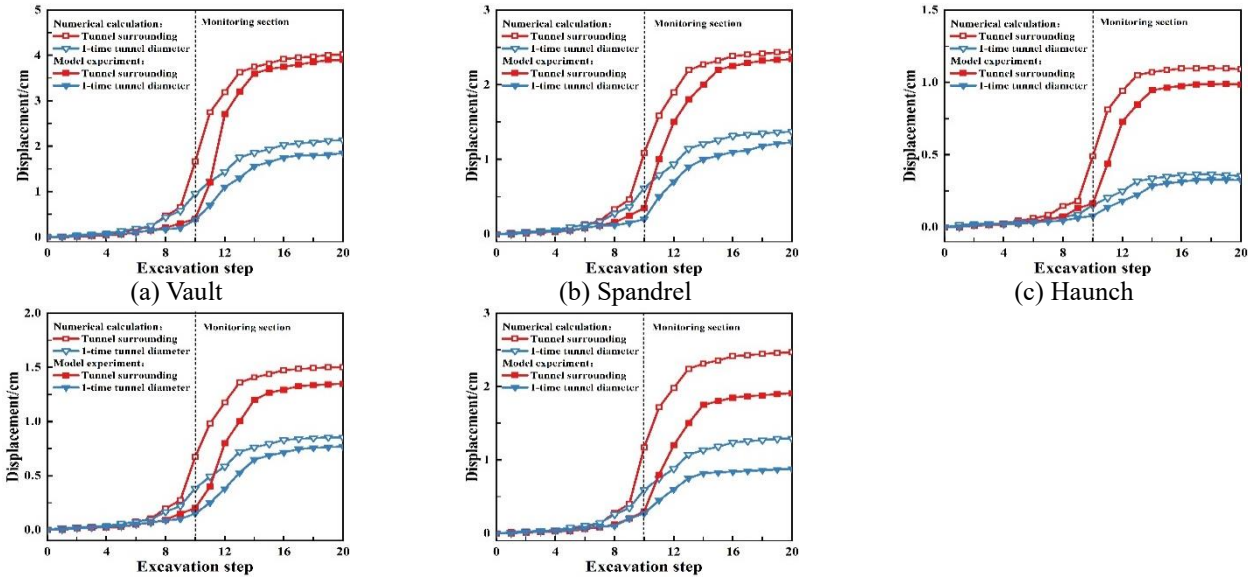

(a) Vault (b) Spandrel (c) Haunch

(d) Foot (e) Bottom

Fig. 19 Displacement comparison curves between numerical simulation and model test results

Table 9 Stress release rate of the surrounding rock in working condition 1

Support method	Location	Vault	Spandrel	Haunch	Foot	Bottom
No support	Around tunnel	84%	15%	52%	-6%	84%
	1-time tunnel diameter	34%	3%	7%	3%	32%
Liner	Around tunnel	73%	13%	34%	-6%	73%
	1-time tunnel diameter	30%	2%	3%	2%	29%
Liner and cable	Around tunnel	74%	-6%	39%	-19%	74%
	1-time tunnel diameter	24%	2%	0%	0%	26%

The numerical simulation results for working condition 1 show the following stress release rates when no support measures are applied: the vault experiences 84%, the spandrel 15.0%, the haunch 52%, and the bottom 84%. The compressive stress at the arch foot increases by 6%. The average stress release rates at one tunnel diameter are: the vault 34%, the spandrel 3%, the haunch 7%, the foot 3%, and the bottom 32%. When only lining support is used, the average stress release rates around the tunnel decrease by 14.8% compared to no support. When both lining and bolt support are used, the average stress release rates decrease by 81.2%.

6.2 Comparison analysis of numerical simulation and model test in working condition 1

The numerical calculation results in Section 5.1 are compared with the model test results in Section 3.4 to verify the accuracy of the model test.

6.2.1 Comparison analysis of displacement results

The displacement comparison results between numerical simulation and model test are shown in Fig. 19.

As illustrated in Fig. 19, the displacement of the surrounding rock observed in the model test closely aligns with the results from the numerical calculations. However, a slight hysteresis is evident in the displacement trend of the model test when compared to the numerical predictions. This delay may be attributed to two factors:

1) The excavation speed is relatively fast, and the next excavation step begins before the surrounding rock has fully deformed.

2) The displacement meters have a certain length, and their placement near the monitoring sections may not be perfectly accurate, leading to small variations in position.

The average discrepancy between the displacement changes observed in the model test and those predicted by the numerical calculations is approximately 12.52%. Specifically, the error for the surrounding rock is 9.03%, while for the rock located one tunnel diameter away, the error is 16%.

Overall, the model test results align well with the numerical calculations. Therefore, the displacement change laws observed in the model test provide valuable engineering insights.

6.2.2 Comparison analysis of stress results

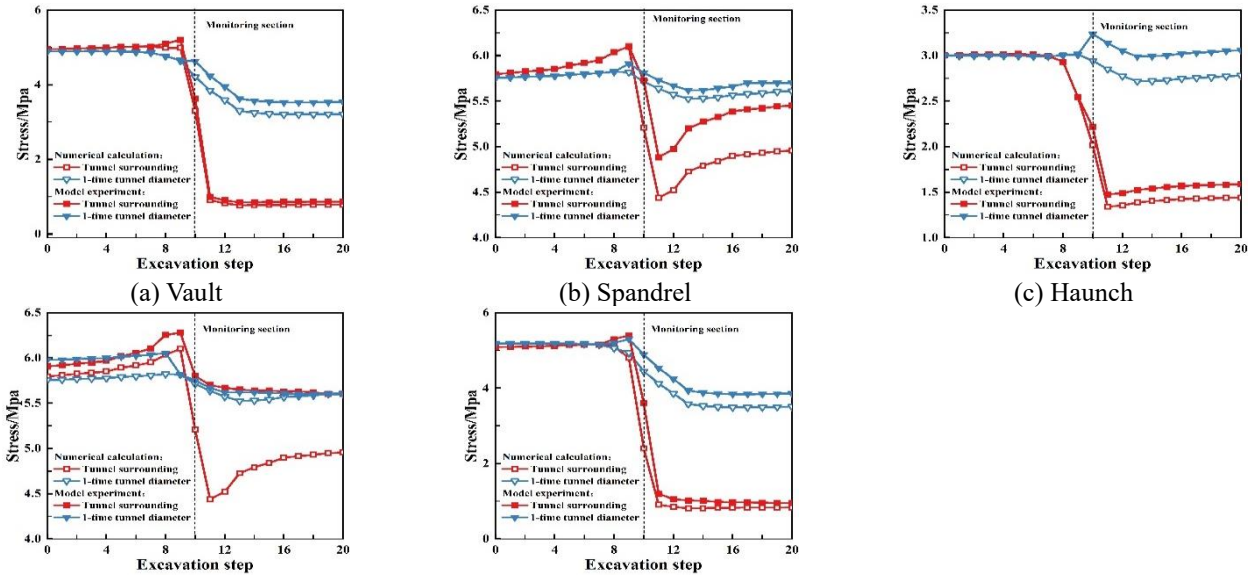

(a) Vault (b) Spandrel (c) Haunch

(d) Foot (e) Bottom

Fig. 20 Stress comparison curves between numerical simulation and model test results: (a) Vault, (b) Spandrel, (c) Haunch, (d) Foot and (e) Bottom

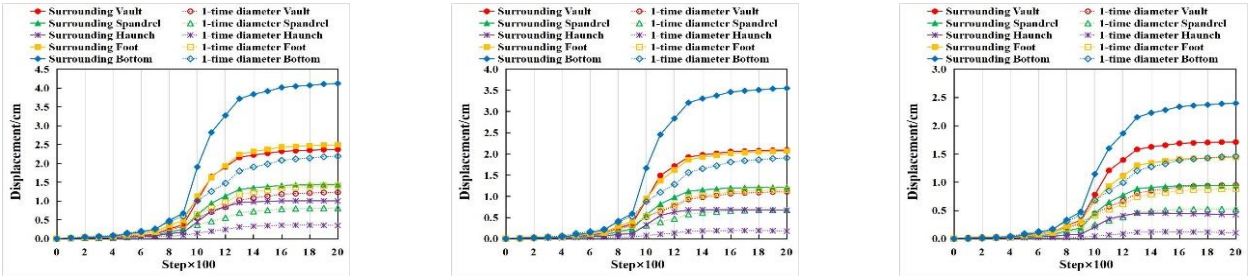

(a) No support (b) Lining support (c) Lining and anchor support

Fig. 21 Displacement curves of the surrounding rock of tunnel excavation in working condition 2

Table 10 Final displacements of the surrounding rock in working condition 2

Support method	Location	Vault (cm)	Spandrel (cm)	Haunch (cm)	Foot (cm)	Bottom (cm)
No support	Around tunnel	2.37	1.44	1.00	2.49	4.12
	1-time tunnel diameter	1.23	0.81	0.35	1.41	2.19
Liner	Around tunnel	2.09	1.22	0.67	2.07	3.55
	1-time tunnel diameter	1.11	0.68	0.18	1.15	1.90
Liner and cable	Around tunnel	1.71	0.94	0.43	1.44	2.40
	1-time tunnel diameter	0.95	0.52	0.10	0.88	1.46

As illustrated in Fig. 20, the stress change patterns of the surrounding rock observed in the model test closely align with those predicted by the numerical simulations. The average error in stress between the model test and the numerical calculations is approximately 7.95%. Specifically, the error for the surrounding rock is 11.9%, while the error for the rock located one tunnel diameter away is 4%.

In conclusion, the model test results demonstrate a strong correlation with the numerical calculations. As a result, the observed stress change patterns in this study offer important reference data for engineering applications.

6.3 Numerical calculation results analysis of the working condition 2

Working condition 2 involves tunnel excavation within a CRL stratum characterized by alternating soft and hard layers. The stratum is composed of 30 meters of hard limestone and 30 meters of soft limestone in the vertical direction. Excavation is carried out under three support scenarios: no support, lining support, and both lining and anchor bolt support.

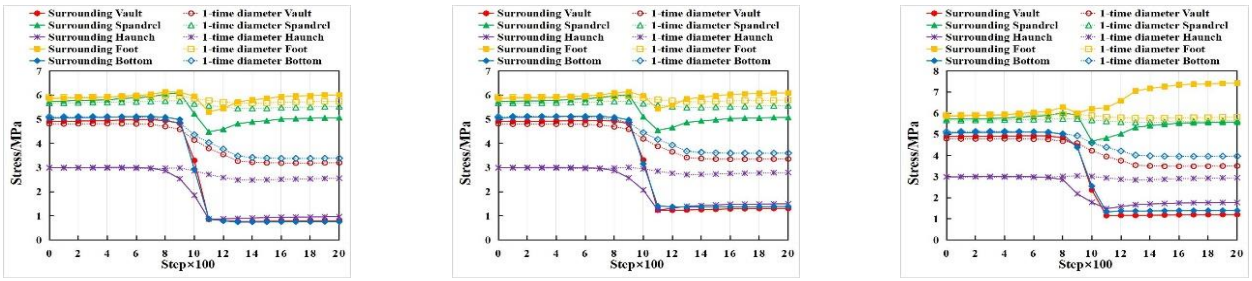

(a) No support (b) Lining support (c) Lining and anchor support

Fig. 22 Displacement curves of the surrounding rock of tunnel excavation in working condition 2

Table 11 Stress release rate of the surrounding rock in working condition 2

Support method	Location	Vault	Spandrel	Haunch	Foot	Bottom
No support	Around tunnel	84%	12%	68%	-3%	85%
	1-time tunnel diameter	34%	3%	14%	3%	34%
Liner	Around tunnel	73%	12%	50%	-4%	73%
	1-time tunnel diameter	30%	2%	7%	2%	30%
Liner and cable	Around tunnel	75%	2%	41%	-27%	72%
	1-time tunnel diameter	27%	0%	1%	2%	23%

6.3.1 Displacement results analysis of the tunnel surrounding rock

The displacement change curves, along with the final displacements at the monitoring points during tunnel excavation, are presented in Fig. 21 and Table 10.

Fig. 21 and Table 10 present the displacement results from the numerical simulation under working condition 2. The displacement of the surrounding rock is most prominent at the arch vault, where hard rock is present, and at the arch bottom, where soft rock is located.

Under working condition 3, when no support measures are applied during tunnel excavation in the CRL stratum, the displacements around the tunnel are as follows: the vault is 2.37 cm, the spandrel is 1.44 cm, the haunch is 1.00 cm, the foot is 2.49 cm, and the bottom is 4.12 cm. The average displacements at one tunnel diameter away are: the vault is 1.23 cm, the spandrel is 0.81 cm, the haunch is 0.35 cm, the foot is 1.41 cm, and the bottom is 2.19 cm.

Compared to no support measures, the average displacement around the tunnel is reduced by 18.2% when only lining support is used, and by 40.8% when both lining and bolt support are applied.

6.3.2 Stress results analysis of the tunnel surrounding rock

The stress change curves and stress release rates of the monitoring points during the tunnel excavation are shown in Fig. 22 and Table 11.

Fig. 22 and Table 11 show the stress release rates from the numerical simulation under working condition 2. When no support measures are applied, the stress release rates around the tunnel are as follows: the vault is 84%, the spandrel is 12%, the haunch is 68%, and the bottom is 85%. The compressive stress at the arch foot increases by 3%. The average stress release rates at one tunnel diameter are: the vault is 34%, the spandrel is 3%, the haunch is 14%, the foot is 3%, and the bottom is 34%.

When compared to no support measures, the average stress release rates around the tunnel are reduced by 17.2% when only lining support is used. When both lining and bolt support are applied, the stress release rates are reduced by 189.8%. The primary reason for this is that the soft rock deformation is significant. As a result, the rock mass at the arch foot is compressed, causing the stress at the arch foot to increase rather than decrease.

7. Conclusions

This study investigates the deformation characteristics and stability of tunnel excavation in the CRL stratum with alternating soft and hard layers. The displacement and stress changes in the surrounding rock are analyzed. The key findings and conclusions are as follows.

- Using similarity theory as a foundation, a mixture of quartz sand, barite powder, high-strength gypsum, and cement is employed to create a similar material that mimics hard CRL rock. To replicate the pore structure characteristics of CRL, prefabricated ice cubes of varying sizes are incorporated during material preparation. The resulting pore structure, created through the ice cube method, exhibits notable inhomogeneity, closely resembling the pore structure of the CRL.
- In the absence of support, the displacement of the soft surrounding rock is 2.6 to 3.6 times greater than that of the hard surrounding rock. When lining support is applied, both the displacement and stress release rate of the surrounding rock decrease by 14.8% and 17.2%, respectively, compared to the no-support scenario. With

the combined use of lining and anchor bolt support, displacement is reduced by 33.3%, and the stress release rate decreases by an average of 29%. In soft limestone areas, the application of support proves more effective in enhancing stability.

- During excavation in the soft upper and hard lower stratum, the soft upper surrounding rock releases stress first, resulting in large displacements at the arch vault and spandrel. As the deformation progresses, the surrounding rock is compressed, with the upper soft rock being pressed by the lower hard rock. This compression can lead to an increase in stress and may trigger failure in the surrounding rock.
- In working condition 2, the arch spandrel experiences elevated lateral pressure due to the weight and displacement of the overlying hard rock. This pressure may cause fracturing or cracking of the hard rock at the arch spandrel. The soft rock at the arch foot is prone to uplifting and lateral displacement due to the loss of support following excavation. The deformation at the arch foot is particularly pronounced due to the relatively poor strength and stability of the soft rock, especially under the weight of the overlying hard rock.
- During tunnel excavation, the surrounding rock at the arch foot is compressed as the arch bottom rises and the haunch converges inward. Rather than releasing stress, the stress at the arch foot increases, leading to stress concentration. The substantial displacement in soft limestone areas exacerbates the stress increase at the arch foot.

Discussion

In the model test, the excavation tool is the Luoyang shovel, the vibration in the excavation process may affect the surrounding rock. Therefore, in order to reduce the disturbance caused by excavation, it is necessary to excavate slowly and a smaller type of the Luoyang shovel is selected.

Neither the model tests nor the numerical simulations in this paper take into account the influence of seawater pressure during the tunnel excavation, which should be given key attention in subsequent research.

Acknowledgments

The research described in this paper was financially supported by the National Key Research and Development Program of China (2023YFC34033500) and the National Natural Science Foundation of China (42107213).

References

Al-Kahtany, K.M. (2017), "Facies development of the Middle Miocene reefal limestone in northwest Saudi Arabia", *J. Afr. Earth Sci.*, **130**, 134-140. https://doi.org/10.1016/j.jafrearsci.2017.03.012.

Bosellini, F.R. (1998), "Diversity, composition and structure of Late Eocene shelf-edge coral associations (Nago Limestone, Northern Italy)", *Facies*, **39**, 203-225. https://doi.org/10.1007/Bf02537017.

Bosellini, F.R., Vescogni, A., Budd, A.F. and Papazzoni, C.A. (2021), "High coral diversity is coupled with reef-building capacity during the late oligocene warming event (Castro Limestone, Salento Peninsula, S Italy)", *Riv Ital Paleontol S*, **127**(3), 515-538. https://doi.org/10.13130/2039-4942/16332.

Burton, C.L., Waltham, A.C. and McLaren, S.J. (2001), "Strength variation in young reef limestones", *Geotechnique*, **51**(10), 887-889. https://doi.org/10.1680/geot.51.10.887.41053.

Chang, J.Q., Thewes, M., Zhang, D.M., Huang, H.W. and Lin, W. (2025), "Deformational behaviors of existing three-line tunnels induced by under-crossing of three-line mechanized tunnels: a case study", *Can Geotech. J.*, **62**, 23-23. https://doi.org/10.1139/cgj-2024-0359.

Chen, Y.J., Liu, M.Y., Yin, F.Q., Zhang, L.W., Wu, J. and Li, J.R. (2024), "Deformation characteristics of surrounding rock in the intersection area between main tunnel and construction adit of the Xianglushan tunnel", *Geomech. Eng.*, **38**(1), 1-13. https://doi.org/10.12989/gae.2024.38.1.001.

He, M.C., Sui, Q.R., Li, M.N., Wang, Z.J. and Tao, Z.G. (2022), "Compensation excavation method control for large deformation disaster of mountain soft rock tunnel", *Int. J. Min. Sci. Technol.*, **32**(5), 951-963. https://doi.org/10.1016/j.ijmst.2022.08.004.

Hu, D., Hu, Y.J., Hu, R., Tan, Z., Ni, P.P., Chen, Y., Xiang, X.J., Li, Y.S. and Liu, J. (2025), "Machine learning-finite element mesh optimization-based modeling and prediction of excavation-induced shield tunnel ground settlement", *Int. J. Comp. Meth.-Sing*, **22**(4). https://doi.org/10.1142/S021987622450066x.

Huang, J., Li, J.Q., Li, M.H., Pan, Y.H. and Zong, Z.H. (2024), "Dynamic response and failure mechanism of ocean coral reef limestone under high strain rate loading", *Ocean Eng.*, **299**. https://doi.org/10.1016/j.oceaneng.2024.117370.

Jafarian, Y., Javdanian, H. and Haddad, A. (2018), "Strain-dependent dynamic properties of Bushehr siliceous-carbonate sand: Experimental and comparative study", *Soil Dyn. Earthq. Eng.*, **107**, 339-349. https://doi.org/10.1016/j.soildyn.2018.01.033.

Li, D.J., Shi, C., Ruan, H.N., Li, B.Y., Li, W.Y. and Yao, X.C. (2022), "Study on shear behavior of coral reef limestone-concrete interface", *Mar. Georesour. Geotechnology*, **40**(4), 438-447. https://doi.org/10.1080/1064119x.2021.1906365.

Li, Z.Q., Nie, L.C., Xue, Y.G., Li, W. and Fan, K.R. (2025), "Model testing on the processes, characteristics, and mechanism of water inrush induced by karst caves ahead and alongside a tunnel", *Rock Mech. Rock Eng.*, **58**(5), 5363-5380. https://doi.org/10.1007/s00603-025-04414-x.

Liu, H.F., Zhu, C.Q., Zheng, K., Ma, C.H. and Yi, M.X. (2021), "Crack initiation and damage evolution of micritized framework reef limestone in the South China Sea", *Rock Mech. Rock Eng.*, **54**(11), 5591-5601. https://doi.org/10.1007/s00603-021-02570-4.

Liu, X.R., Suliman, L., Zhou, X.H., Zhang, J.L., Xu, B., Xiong, F. and Abd Elmageed, A. (2022), "The difference in the slope supported system when excavating twin tunnels: Model test and numerical simulation", *Geomech. Eng.*, **31**(1), 15-30. https://doi.org/10.12989/gae.2022.31.1.015.

Luo, Y., Gong, H.L., Wei, X.Q., Zheng, S.L., Pei, C.H. and Li, X.P. (2023), "Dynamic compressive characteristics and damage constitutive model of coral reef limestone with different cementation degrees", *Constr. Build. Mater.*, **362**. https://doi.org/10.1016/j.conbuildmat.2022.129783.

Meng, Q.S., Wu, K., Zhou, H.R., Qin, Q.L. and Wang, C. (2022), "Mesoscopic damage evolution of coral reef limestone based on real-time CT scanning", *Eng. Geol.*, **307**.

https://doi.org/10.1016/j.enggeo.2022.106781.
Nakamori, T., Iryu, Y. and Yamada, T. (1995), "Development of coral-reefs of the Ryukyu Islands (Southwest Japan, East-China-Sea) during pleistocene sea-level change", *Sediment Geol.*, **99**(3-4), 215-231. https://doi.org/10.1016/0037-0738(95)00045-A.
Pei, C.H., Li, X.P., Ma, R.Q., Luo, Y. and Zhang, C. (2022), "Research on the dynamic fracture toughness of reef limestone", *Ocean Eng.*, **264**. https://doi.org/10.1016/j.oceaneng.2022.112387.
Raczynski, P., Peryt, T.M. and Strobel, W. (2017), "Sedimentary and environmental history of the Late Permian Bonikowo Reef (Zechstein Limestone, Wuchiapingian), western Poland", *J. Palaeogeog-English*, **6**(3), 183-205. https://doi.org/10.1016/j.jop.2017.05.001.
Seo, S. and Chung, M. (2023), "Polynomial model controlling the physical properties of a gypsum-sand mixture (GSM)", *Geomech. Eng.*, **35**(4), 425-436. https://doi.org/10.12989/gae.2023.35.4.425.
Sun, X.M., Jiang, M., Miao, C.Y., Wang, J. and Zhang, J.X. (2023), "Study on large deformation and failure mechanism of deep buried stratified slate tunnel and control strategy of high constant resistance anchor cable", *Eng. Fail. Anal.*, **144**. https://doi.org/10.1016/j.engfailanal.2022.106953.
Tang, H.D. and Zhu, M.L. (2025), "A Nonlinear Breakage Mechanics Model: From Extreme Entire Life Model to Breakage Evolution of Limestone Based on Separation of Helmholtz Free Energy under Cyclic Loading", *Int J Geomech*, **25**(2). https://doi.org/10.1061/Ijgnai.Gmeng-10244
Triantafyllidis, T. and Kimmig, I. (2019), "A simplified model for vibro compaction of granular soils", *Soil Dyn. Earthq. Eng.*, **122**, 261-273. https://doi.org/10.1016/j.soildyn.2018.12.008.
Wan, Z.H., Dai, G.L. and Gong, W.M. (2018), "Full-scale load testing of two large-diameter drilled shafts in coral-reef limestone formations", *Bull. Eng. Geol. Environ.*, **77**(3), 1127-1143. https://doi.org/10.1007/s10064-017-1206-1.
Wang, J.C., Wang, C.Y., Han, Z.Q., Wang, Y.T. and Zou, J.P. (2023a), "3D reconstruction and characterization of reef limestone pores based on optical and acoustic microscopic images", *Mar. Georesour. Geotec.*, **41**(9), 1038-1052. https://doi.org/10.1080/1064119x.2022.2116371.
Wang, J.Y., Li, W.J., Rui, R., Zhai, Y.X. and He, Q. (2023b), "Experimental investigation of earth pressure on retaining wall and ground settlement subjected to tunneling in confined space", *Geomech. Eng.*, **32**(2), 179-191. https://doi.org/10.12989/gae.2023.32.2.179.
Wang, X.Z., Wang, X., Shen, J.H., Ding, H.Z., Wen, D.S., Zhu, C.Q. and Lv, S.Z. (2022), "Foundation filling performance of calcareous soil on coral reefs in the South China Sea", *Appl. Ocean Res.*, **129**. https://doi.org/10.1016/j.apor.2022.103386.
Wild, C., Hoegh-Guldberg, O., Naumann, M.S., Colombo-Pallotta, M.F., Ateweberhan, M., Fitt, W.K., Iglesias-Prieto, R., Palmer, C., Bythell, J.C., Ortiz, J.C., Loya, Y. and van Woesik, R. (2011), "Climate change impedes scleractinian corals as primary reef ecosystem engineers", *Mar. Freshwater Res.*, **62**(2), 205-215. https://doi.org/10.1071/Mf10254.
Wu, Y., Wang, X., Shen, J.H., Cui, J., Zhu, C.Q. and Wang, X.Z. (2020), "Experimental study on the impact of water content on the strength parameters of coral gravelly sand", *J. Mar. Sci. Eng.*, **8**(9). https://doi.org/10.3390/jmse8090634.
Wu, Z.Y., Yu, H.F., Ma, H.Y., Zhang, J.H. and Da, B. (2023), "Physical and mechanical properties of coral aggregates in the South China Sea", *J. Build. Eng.*, **63**. https://doi.org/10.1016/j.jobe.2022.105478.
Xu, D.S., Zhang, S.S. and Qin, Y. (2024), "Study of the micromechanical properties and dissolution characteristics of porous coral reef limestone", *J. Geophys. Res. Solid Earth*, **129**(11). https://doi.org/10.1029/2024JB029131.
Xu, D.S., Zhao, Y.M., Liu, H.B. and Zhu, H.H. (2017), "Deformation monitoring of metro tunnel with a new ultrasonic-based system", *Sensors-Basel*, **17**(8). https://doi.org/10.3390/s17081758.
Ye, J.H., Shan, J.P., Zhou, H.R. and Yan, N.X. (2021), "Numerical modelling of the wave interaction with revetment breakwater built on reclaimed coral reef islands in the South China Sea-Experimental verification", *Ocean Eng.*, **235**. https://doi.org/10.1016/j.oceaneng.2021.109325.
Yin, Q., Zhou, Y. and Rao, J.Y. (2025), "An intelligent prediction method for surface settlement of shield tunnel construction based on CNN-BiLSTM-SA", *Ksce J. Civil Eng.*, **29**(4). https://doi.org/10.1016/j.kscej.2024.100061.
Zhang, H., Ren, H.Q., Mu, C.M., Wu, X.Y., Huang, K., Zhang, H.E. and Wang, F. (2023a), "Experimental study on dynamic mechanical properties and damage characteristics of coral reef limestone", *Constr. Build. Mater.*, **384**. https://doi.org/10.1016/j.conbuildmat.2023.131007.
Zhang, M.C., Luo, Y., Gong, H.L., Zhu, Y.W. and Li, X.P. (2024), "Fine characterization of pore structures in coral reef limestones based on three-dimensional geometrical reconstruction", *Mar.Georesour. Geotechnol.*, **42**(6), 721-735. https://doi.org/10.1080/1064119x.2023.2215246.
Zhang, S.L., Bao, T. and Liu, C. (2023b), "Model tests and numerical modeling of the failure behavior of composite strata caused by tunneling under pipeline leakage conditions", *Eng. Fail. Anal.*, **149**. https://doi.org/10.1016/j.engfailanal.2023.107287.
Zhang, X.Y., Zhang, L.W., Wu, J., Fu, H. and Dian, L.Y. (2022a), "Tunnel stability analysis of coral reef limestone stratum in ocean engineering", *Ocean Eng.*, **265**. https://doi.org/10.1016/j.oceaneng.2022.112636.
Zhang, Y. and Ye, J.H. (2021), "Physical modelling of the stability of a revetment breakwater built on reclaimed coral calcareous sand foundation in the South China sea-random waves and dense foundation", *Ocean Eng.*, **219**. https://doi.org/10.1016/j.oceaneng.2020.108384.
Zhang, Y.T., Deng, Z.Q., Chen, P.S., Luo, H.W., Zhang, R.Y., Yu, C.C. and Zhan, C.Z. (2022b), "Experimental and numerical analysis of pile-rock interaction characteristics of steel pipe piles penetrating into coral reef limestone", *Sustainability-Basel*, **14**(21). https://doi.org/10.3390/su142113761.
Zhang, Z.Q., Chen, F.F., Li, N., Swoboda, G. and Liu, N.F. (2017), "Influence of fault on the surrounding rock stability of a tunnel: Location and thickness", *Tunn. Undergr. Sp. Tech.*, **61**, 1-11. https://doi.org/10.1016/j.tust.2016.09.003.
Zhao, Z.L., Jing, H.W., Shi, X.S., Yang, L.J., Yin, Q. and Gao, Y. (2021), "Study on bearing characteristic of rock mass with different structures: Physical modeling", *Geomech. Eng.*, **25**(3), 179-194. https://doi.org/10.12989/gae.2021.25.3.179.
Zhong, Y., Li, Q., Wang, R. and Yao, T. (2022), "Changes of physical and mechanical properties of coral reef limestone under CO-seawater-rock interaction", *Appl. Sci.-Basel*, **12**(9). https://doi.org/10.3390/app12094105.
Zhou, J., Ding, Z., Huang, J.K., Yang, X.A. and Ma, M.J. (2024), "The tunnel model tests of material development in different surrounding rock grades and the force laws in whole excavation-support processes", *Geomech. Eng.*, **36**(1), 51-69. https://doi.org/10.12989/gae.2024.36.1.051.
Zhu, W.S., Li, S.C., Li, S.C., Chen, W.Z. and Lee, C.F. (2003), "Systematic numerical simulation of rock tunnel stability considering different rock conditions and construction effects", *Tunn. Undergr. Sp. Tech.*, **18**(5), 531-536. https://doi.org/10.1016/S0886-7798(03)00070-1.